THE JOURNAL OF
PHYSICAL CHEMISTRY A

Article

pubs.acs.org/JPCA

Infrared Spectral Model for Subwavelength Particles of Mixed Composition based on the Spectra of Individual Particles with Calibration Data for Airborne Dust

David B. Lioi, Katherine E. Cilwa, Matthew McCormack, Marvin A. Malone, and James V. Coe*

Department of Chemistry and Biochemistry, The Ohio State University, 100 West 18th Avenue, Columbus, Ohio 43210-1173, United States

Supporting Information

ABSTRACT: A Mie−Bruggeman spectral model is presented which predicts the orientationally averaged, infrared spectra of individual mixed-composition particles or the average spectrum of collections of such particles. The model uses parameters extracted from sets of individual particle spectra of pure materials known to be in subject mixtures. The spectra of both calibrants and subject particles were recorded by trapping size-selected particles in the holes of plasmonic metal mesh. Calibrating data is presented for quartz, calcite, dolomite, three clays, gypsum, polyethylene, and living organic material (yeast cells). The individual particle spectra of these calibrants are averaged to account for crystal orientation effects, fit by a Mie theory model, and tabulated herein as dielectric functions of each component. The component dielectric functions are combined in this model with Bruggeman effective medium theory producing a spectral prediction for mixed-composition particles. The Mie−Bruggeman model was used to analyze the composition of dust from our lab air [K. E. Cilwa et al. *J. Phys. Chem. C* **2011**, *115*, 16910] based on the average spectrum of the dust particles. The model does a reasonable job of characterizing the dust in our laboratory air exhibiting promise for future applications. This work presents the model and illustrates potential; however, much more work will be required before its accuracy as a quantitative analytical method is established.

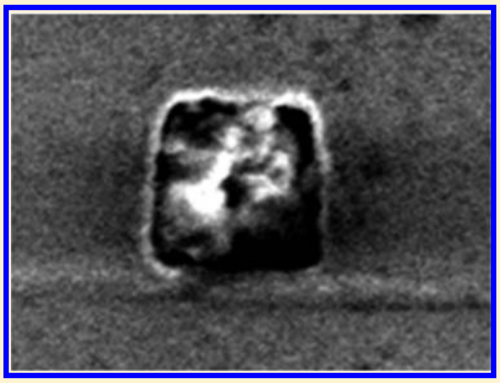

INTRODUCTION

This work proposes a model for predicting the infrared (IR) spectra of mixed composition particles. Since the model combines Mie theory[1,2] with Bruggeman effective medium theory,[3] it has been called a Mie−Bruggeman model. It predicts the orientationally averaged, infrared spectra of individual mixed-composition particles or the average spectrum of collections of such particles. The model requires calibration in the form of spectra of individual pure particles that are known to be in the particle mixture of interest. The model is general, but the calibration is specific to a sample of interest.

In order to show that the model is useful, it has been applied to previous work on dust from our laboratory air.[4] Airborne particulate matter typically consists of individual particles that are mixtures of many materials.[5,6] The particles vary in size and shape, include mineral and organic components, and are often similar in size to the wavelength of probing light. These attributes combine to make the prediction of the spectra of mixed-composition particles challenging. Airborne particulate matter is important in a variety of fields including astronomy,[7−12] geology,[7] atmospheric and environmental sciences,[13−17] and human health.[18−22] While airborne particles are mostly natural, ~6−23% are thought to be anthropogenic[5] and therefore diagnostic for human effects on the environment. Increases in particulate matter are correlated with asthma, bronchitis, silicosis, asbestosis, pneumonia, lung cancer, and cardiovascular diseases.[5] Actuarial information also indicates that particulate matter increases are correlated with a general increase in human mortality[20] of all causes. While the case is clear for regulating particulate matter smaller than 2.5 μm ($PM_{2.5}$), there is a need for more definitive results[19−21] regarding the US Environmental Protection Agency's current 24 h standard (150 $\mu g/m^3$) for particulate matter smaller than 10 μm (PM_{10}). The size regime from 2.5 to 10 μm contains the largest globular particles that get past our noses and throats,[6] making it into our lungs. Particles of the size of this work (~4 μm diameter) may be better correlated with local environmental hazards as they do not travel in the air as far as nanoparticles. As an example, it is interesting that there is much silica in our inhalable dust[4] since silicosis is a disease associated with miners and glassblowers who are exposed to excessive amounts of silica particles. Knowledge of the volume fraction of these materials in laboratory air, assumed to be benign, will aid in the establishment of safety standards for particulate matter based on composition rather than just size. Noting studies that establish strong correlations with specific atoms in the particulate matter,[19] it is clearly desirable to know the chemical

Received: June 6, 2013
Revised: October 8, 2013
Published: October 8, 2013

compounds associated with these elements, an area where infrared (IR) spectroscopy can be very useful.

The Coe Group has recorded IR spectra of individual subwavelength particles including live yeast cells,[23] latex microspheres,[24,25] and dust particles[4,26] by using plasmonic Ni films with arrays of subwavelength holes[27−30] and an imaging FTIR microscope. Scanning electron microscope images of dust particles trapped in the holes of plasmonic mesh are given in Figure 1. Recently, we published a library of 63 "scatter-free" infrared spectra of individual airborne dust particles from our laboratory air[4] (from room 0055 of Evans Lab on the campus of the Ohio State University). The particles were obtained on April 21, 2010, which was a clear day, with an average temperature of 12 °C and an average relative humidity of 47%. The spectra are available in a supplement[4] for any and all to analyze. The dust was mainly composed of minerals such as quartz, clay, carbonate, sulfates (primarily gypsum), and nitrates, as well as a high occurrence of organic material.

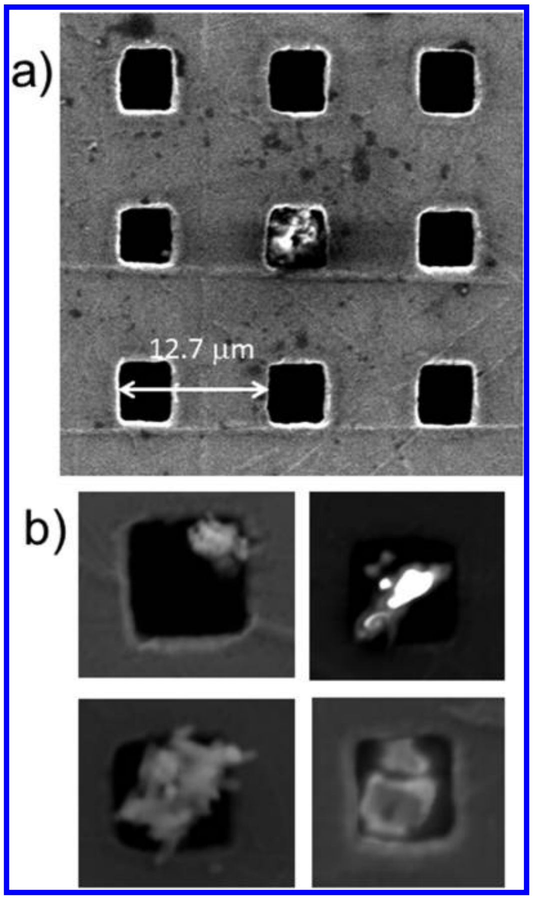

Figure 1. Scanning electron microscope (SEM) images of dust particles from our laboratory air caught in the holes of Ni plasmonic metal mesh (12.7 μm lattice parameter, ~5 μm square hole width, ~ 2 μm thick) by pumping air through the mesh. (a) Collection is refined to produce particles surrounded by empty holes to isolate the single particle spectra. (b) Although dust particles are often insulating, nearness to the metal of the hole controls charging sufficiently for SEM images, i.e., these particles are not Au coated. These are not the dust particles from our earlier studies. They show that typical dust particles are not spherical illustrating the need for averaging in this work.

The work of Hobert,[31] who collected dust at the top of the tallest building in Jena Germany and pressed it into KBr pellets, is instructive. His IR spectra and principle component analysis identified many of the mineral components in airborne dust, but it did not quantify them. Individual dust particle spectra from our lab air exhibited many narrow, crystalline IR bands for minerals, which would be averaged-away if bulk samples were pressed into KBr pellets. Differences of individual particle spectra from bulk powder spectra suggest the potential to extract different information. More generally, the spectra of homogeneous powders pressed into KBr pellets can vary dramatically because the samples correspond to different particle size distributions, different amounts of air between particles, and many particles of comparable size to the wavelength of probing light. The latter causes line shape distortions, which vary with particle size and shape.[1,32] For example, if you compare the IR band strengths from dielectric functions of pure calcite crystals with those of a pressed pellet of calcite,[33] they do not agree. Without extensive knowledge of the size distributions, air or packing, and the particle shapes of a powder, the quantitative connection to the amount of components is lost. Our new Mie−Bruggeman model (featuring data from a new experimental technique (scatter-free IR spectra of individual micrometer-sized particles), shows how individual particle data can be used to establish the quantitative connection.

Another advantage of an approach based on individual particle spectra involves the organic components. It was difficult, in the pressed pellet work of Hobert, to find any organic peaks other than the CH_2 stretches of hydrocarbon chains at 2859 and 2915 cm^{-1}, and consequently, little was learned about organic constituents. The library of individual dust particle spectra from our lab air shows many spectra with organic bands other than CH_2 stretches allowing the start of more in-depth studies of the organics.[34] Unlike minerals, the organic molecules in dust potentially represent millions of different molecules, so our strategy is to find different groups of organics. This work only has two groups of organics including recently living biomatter (based on our studies of live yeast cells) and hydrocarbon chains (the only organics observed by Hobert). Certainly more groups of organics are needed. We assert that organic matter experiences a progression of decay that is evident on airborne lab dust ranging from living organic matter and extending to the geological end product of pure hydrocarbons.[35]The current work and model only represent a first step down the road to understanding the progression of organic material on airborne dust. Work continues on organics, and new calibrants will be added to the model in the future.

Traditional infrared spectra have a range of ~500−4000 cm^{-1} (or ~20−2.5 μm), which overlaps the size range of particles studied in this work. Particles the same size as probing light have a number of complicating effects including[1,2,26,36] (1) dominant generic scattering with a broad Mie-like spectrum, (2) composition consisting of mixtures of a variety of mineral and organic components, (3) many crystalline components (whose effects are averaged-away in bulk dust samples), (4) irregular globular shapes that can change phonon lineshapes, (5) dispersive phonon band phase and line shape distortions, (6) dispersion shifts of bands with orientation, (7) crystalline orientation effects like bi- or trirefringence, and (8) phonon line shape distortions due to very strong bands that vary with particle size.[32] The use of plasmonic mesh helps to reduce the effects of scattering and dispersive line shape distortions,[37] and the large range of angles employed in the objectives (Cassegrain optics) of commercial IR microscopes also helps to average away some of the crystal orientation effects. The remaining orientation problems were addressed by the averaging of individual spectra, both for the calibrants and dust particle library.

In our single particle experiments, there is no control over the orientation adopted by a particle as it is trapped. In contrast, literature experiments on crystals typically introduce light along a high symmetry plane or axis of the crystal. As already mentioned, spectra of powders have some of the averaging effects desired in this work, but they also have spaces between the particles and distributions of particle sizes and shapes, which alter the effective dielectric function and its corresponding spectrum. Anisotropic crystalline materials have specific directions for the phonon transition moments. For example, birefringent crystals (such as quartz or calcite) have vibrations that are classified into two separate groups (ordinary and extraordinary or, more formally, by the corresponding symmetry of the phonon groups) with perpendicular transition moments. Trirefringent crystals (like clay) have three different groups of phonons. Consequently, the spectra of randomly oriented crystals can be significantly different than those of literature reports. For example, they might include bands that have little intensity upon incidence of light from high symmetry directions. As a result, the spectra of 94 calibrating dust particles were recorded under the same conditions as our lab air dust particles, i.e., with a well-defined microscope window, which can be used to obtain absolute cross-sections. In this way the calibrating spectra had all of the same problems of particles of similar size to the probing light as does our dust library. First, the individual particle spectra of these calibrants (including three types of clay, gypsum, calcium carbonate, dolomite, quartz, polyethylene, and individual live yeast cells) were averaged to account for crystal orientation effects, fit by a Mie theory model, and tabulated herein as dielectric functions of each component (a vibrationally modified permittivity or dielectric function). Then, a model from Bruggeman effective medium theory was developed to obtain the permittivity of a particular mixture of the calibrants. The utility of the model is demonstrated by simulating the average spectrum of the library of 63 dust particles from our lab air. Ultimately, we aim to develop a model that incorporates random orientation of a single particle. In the meantime, our Mie−Bruggeman model uses particle spectra averaging and extracts estimates of the volume fractions of the various dust components in spite of the fact that airborne dust is a complex mixture of a large number of components. The tables of dielectric function parameters provided for each calibrant and our model enable the prediction of the extinction and/or absorption spectra of mixed particles of other sizes than those used to generate the data, hence the utility in a variety of other fields studying dust. While our results pertain to a size range associated with the largest inhalable particles, others may use the method for particles of different sizes or even distributions of sizes. The main contribution of this work is in allowing for arbitrary mixtures of the subject components within a particle. Please note that the current model's results are averaged over orientation and so pertain to either single, isotropic, spherical particles, or averages of nonspherical, anisotropic single particle sets. This is a good starting point for studies of mixed particles that are not spherical.

■ EXPERIMENTAL SECTION

The 94 calibrating particles and all 63 dust particles from lab air[4] were analyzed in the same way, so their intensities are meaningful in absolute terms, as well as relative to each other. The techniques employed here have been described in detail elsewhere.[4,23,24,26] Briefly, the dust particles from our lab air were obtained by pumping lab air through a plasmonic metal mesh (12.6 μm square lattice parameter, ~5 μm square holes, thickness of ~2 μm, available in Ni from Precision Eforming) at 5.0 L/min for 18 h with no further processing (such as drying). The calibrant powder is first ground into a fine powder with a mortar and pestle before being placed on the plasmonic mesh with house vacuum applied from beneath the mesh. The mesh itself is taped onto an aluminum washer with a 1/8″ (3.18 mm) diameter hole in the center. The powder is mechanically agitated by sharply tapping the washer's side and then the powder is brushed aside. The mesh was placed under an optical microscope (Olympus B50, 50×) to tell if a working number of particles were trapped and suitably isolated with empty holes. A particle was considered sufficiently isolated when all of the neighboring holes were empty. Most had many more empty holes than the minimum. If there were not enough candidate particles, the procedure was repeated.

IR spectra were recorded with a Perkin-Elmer Spotlight 300 imaging FTIR microscope system with an array of 16, liquid-nitrogen-cooled, Mercury Cadmium Telluride (MCT) detectors. Spectra were recorded in imaging mode (700−4000 cm^{-1} range, 4 cm^{-1} resolution, 6.25 μm by 6.25 μm pixels on a square grid, 512 scans per pixel). The window at the focal plane of the microscope is imaged with a magnification of ~5.4 onto an array of 16 MCT detectors (each of rectangular shape, simultaneously recording spectra). Imaging is accomplished by programmed stepping of the sample holder beneath the fixed optical system. The result of this optical arrangement is that each detector in the array senses a region that corresponds to a square of 6.25 μm by 6.25 μm in the original focal plane of the microscope's window, i.e., an image pixel. After obtaining the full imaging data set, software enables selection of rectangular subset regions within the microscope window. In this case, the subset regions consist of 9 pixels in a 3 pixel by 3 pixel array, i.e., a 18.75 μm by 18.75 μm region, which is centered on the particle. There is always one full hole containing a particle near the center. There are also a set of 8 surrounding empty holes making variable fractional contributions within the 3 pixel by 3 pixel region whose contributions always add up to ~1.2 holes. For analysis, a 3 pixel by 3 pixel box was drawn around the dust particle in the microscope image, and all transmission spectra within the box were averaged; then the same size box was centered about a nearby empty hole, and all transmission spectra within were coadded. Finally, the averaged transmission spectrum of the dust particle was divided by that of the empty hole, and the result was converted to absorbance units. Previous experiments with single 5.0 μm latex spheres[23] show that the box acts like an effective window that is 19.3 μm by 19.3 μm allowing conversion to absolute cross-section units. The scanning time for a single particle with 512 scans/pixel, perfect alignment (the IR beams are rarely perfectly aligned with the optical images in these microscopes), and a minimum of pixels for both the particle and an empty hole is ~30 min. In practice, it is more efficient to scan large windows with multiple, isolated particles requiring ~5 h of time, but not the operator's presence.

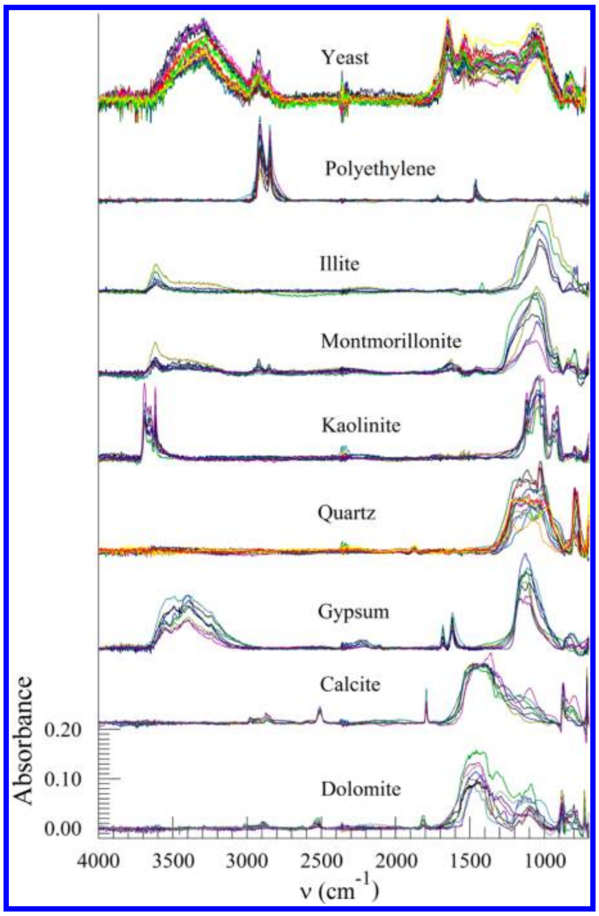

Figure 2. IR scatter free spectra of 94 particles representing 9 groups of calibrants that have been trapped in the holes of Ni plasmonic mesh. The particles vary from about 3−5 μm in width. While the polyethylene is best behaved as a calibrant because it comes from amorphous and monodisperse spherical particles, most of the mineral calibrants exhibit variations due to a distribution of particle size and orientation. In addition, the strongest bands often show the greatest variations as they suffer from particle saturation effects because their phonon band cross-sections are comparable to the physical cross-section of the particles.

Spectra were recorded for 94 calibrant particles of 9 different calibrants whose individual spectra are shown in Figure 2. The digital data for each spectrum has been made available in a supplementary text file for those who might want to try different approaches. The calibrants include crystalline α-quartz (crushed from a quartz crystal, SiO_2), calcium carbonate (Fisher Scientific, $CaCO_3$), dolomite (from rock samples, $Ca_{0.5}Mg_{0.5}CaCO_3$), gypsum (Fisher Scientific, $H_2SO_4.2H_2O$), three types of clays (kaolinite, Illite, and montmorillonite), live yeast cells[23] (Fleischmann's bread yeast, *Saccharomyces cerevisiae*), and polyethylene spheres [Cospheric Co., $CH_3(CH_2)_{n\approx40}CH_3$]. Three specific clays representing three general types of clay were acquired from the Clays Repository (www.clays.org). The kaolinite (sample KGa-1b from Washington Co. Georgia) has the formula $Al_2Si_2O_5(OH)_4$ and is the most ordered structure of the clays exhibiting fairly narrow bands across its IR spectrum. Montmorillonite (STx-1b from Gonzales Co. Texas) has the formula $(Na,Ca)_{0.33}(Al,Mg)_2Si_4O_{10}(OH)_2{\cdot}nH_2O$, while Illite (IMt-1, Cambrian shale from Silver Hill Montana) has the formula $(K,H_3O)(Al,Mg,Fe)_2(Si,Al)_4O_{10}[(OH)_2,(H_2O)]$. The latter two clays represent a large set of clays with a variety of cation substitutions causing broader OH^- bands and a combination of OH^- and H_2O stretching vibrations. These spectra have been baseline corrected in order to remove a generic rise in the baseline from low to high wavenumbers. This effect arises due to the globular nature of the particles, which causes them to have some lensing (like a sphere) as the value of the dielectric function increases with increasing wavenumbers (an increasing fraction of light at higher wavenumbers is lost from the detector). The variations in the calibrating spectra of Figure 2 are not random statistical fluctuations. They arise from changes due to orientation, small changes in the effective radius, and the effect of strong phonons whose cross-sections approach the geometrical cross-sections of the particles. Averaging is used to address these effects in the next section and to obtain Mie fits and vibrationally mediated dielectric functions for each calibrant.

■ MIE FIT RESULTS FOR CALIBRANTS

The average IR spectrum of each calibrant and a best nonlinear least-squares fit based on Mie theory are given in Figure 3. Mie theory is used to model the spectra of small, spherical,

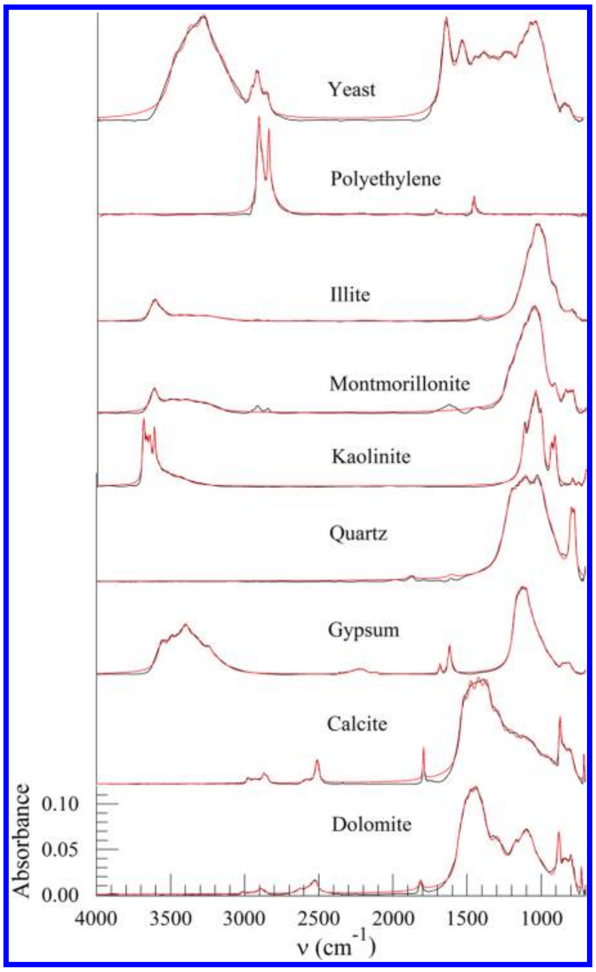

Figure 3. Average spectrum (black trace) of each set of individual particles for each calibrant has been fit with a Mie model to obtain the red traces. The fits can be reproduced with the dielectric function parameters [see eq 3] given in Tables 1−9. Averaging is the key to dealing with various particle effects.

homogeneous particles comparable in size to the wavelength of light. It was developed in 1908 by Gustav Mie, but we have used the formulations of Bohren and Huffman[1] and van de Hulst.[2] If one had the three-dimensional shapes of randomly oriented particles (which we do not, even with SEM images), and the shapes were all overlaid at a common origin of the center of mass of each particle (exceedingly difficult to arrange), and then one averaged the distance from center to particle edge over all particles at all solid angles, we claim (and this model assumes) that this will tend in general toward a spherical shape. Averaging many single particle spectra makes the spherical assumptions of Mie theory work much better than it would for a single particle. One inputs the particle radius (r) and complex index of refraction (m) and the output is a series solution to Maxwell's equations yielding complex Mie coefficients. The extinction and scattering cross-sections are expressed in terms of these coefficients as

$$C_{\text{ext}} = \frac{1}{2\pi\tilde{\nu}^2} \sum_{n=1}^{\infty} (2n+1)\boldsymbol{Re}(a_n + b_n) \tag{1}$$

$$C_{\text{sca}} = \frac{1}{2\pi\tilde{\nu}^2} \sum_{n=1}^{\infty} (2n+1)(|a_n|^2 + |b_n|^2) \tag{2}$$

where a_n and b_n are the complex Mie coefficients, and $\boldsymbol{Re}$ is the real function. The absorption cross-section is $C_{\text{abs}} = C_{\text{ext}} - C_{\text{sca}}$, so the method reduces to finding the Mie coefficients numerically. A program was written in Fortran using Bohren and Huffman's[1] well-known subroutine (appendix of 1987 edition gives Fortran code) without modification. Since our model calculates in cross-section units and spectra are measured in absorbance units, a common empirical scaling factor (6.80×10^{-7} cm^2)[23] was used to convert absorbance to absolute cross-section units (cm^2). Vibrational bands (lattice phonons or molecular modes) are managed by adding damped harmonic oscillator terms to the complex dielectric function, ε, for each vibration. This strategy for lattices is also known as classical dispersion theory. It gives rise to Lorentzian lineshapes in absorption spectra, dispersive lineshapes in scattering spectra, and combinations in extinction spectra. The complex index of refraction, m, needed for Mie theory is obtained from the complex dielectric function, ε, as

$$m^*(\tilde{\nu}) = \sqrt{\varepsilon(\tilde{\nu})} = \sqrt{\varepsilon_0 + \sum_j \frac{A_j \tilde{\nu}_{0,j}^{\,2}}{\tilde{\nu}_{0,j}^{\,2} - \tilde{\nu}^2 - i\Gamma_j \tilde{\nu}}} \tag{3}$$

where ε_0 is the constant, generic part of the complex dielectric function, j is an index over the vibrations, A_j is the unit-less strength of the vibrational transition, $\tilde{\nu}_{0,j}$ is the position of the transition in wavenumber units, and Γ_j is the full-width-at-half-max of the resonance in wavenumber units. The parameters, $\tilde{\nu}_{0,j}$ and Γ_j, are the same as would be used with a Lorentzian function; however, intensities are more complicated (all three of these vibrational parameters are important when comparing to traditional approaches of orientation-averaged intensities such as Beer's Law extinction coefficients or integrated band intensities). Equation 3 gives m^* rather than m because the Bohren and Huffman routine requires the complex conjugate of this index of refraction in order to work properly. The parameters, $\tilde{\nu}_{0,j}$, A_j, and Γ_j are the position, strength, and width parameters, respectively, of each phonon, which are fit by a home-written nonlinear least-squares Fortran routine that used a simple grid search technique as described by Bevington.[38] The resulting fits are shown in Figure 3 and Tables 1−9 with some assignments from the literature.

The Mie fit parameters of the average α-quartz (SiO$_2$) particle spectrum are given in Table 1. The α-quartz crystal is uniaxial giving it birefringent optical properties, which were addressed herein by averaging. It has been studied extensively in the IR,[39−44] was detected in 53% of our laboratory air particles,[4] and is well-known in dust.[31,45] The unit cell (9 atoms) has 27 fundamental vibrations of which 10 are active in the IR (four doubly degenerate E symmetry vibrations and two A$_2$ vibrations). All are evident in our average spectrum (see Table 1). Our single particle technique is sufficiently sensitive to detect combination bands and overtones, which account for some of the unassigned peaks.[46] Since the individual particles are randomly oriented, there can also be dispersion shifts or broadening and simultaneous observation of transverse optical (TO) and longitudinal optical (LO) peaks. The strongest peaks at ~1000 cm^{-1} are also subject to particle saturation effects, i.e., line shape broadening and distortion, which occur due to a band intensity (when expressed in cross-section units) being comparable to the physical cross-section of the particle.[32]

Table 1. α-Quartz Mie Fit Parameters of the Average of 15 Particle Spectra with Estimated Standard Deviations in Parentheses As Least Significant Figures; if There Is No Error, Then the Parameter Was Fixed; the Fitted Radius Was 1.9048(7) μm and ε_0 = 2.365

ν (cm^{-1})	A	Γ (cm^{-1})	assignment/experimental ν (cm^{-1})[44]
697	0.0047(7)	2.6(5)	E 695(TO), E 697.6(LO)
776.79(18)	0.01477(18)	20.0(4)	A$_2$ 777(TO), A$_2$ 790(LO)
796.68(18)	0.01963(19)	27.2(4)	E 797(TO), E 810(LO)
937.9(7)	0.0389(3)	131.3(13)	
1007.0(3)	0.0367(2)	80.1(7)	A$_2$ 1071(TO)
1050.1(5)	0.02081(19)	73.0(9)	E 1065(TO)
1103.2(3)	0.02333(17)	67.5(7)	
1149.7(4)	0.01761(15)	67.6(8)	E 1158(TO), E 1155(LO)
1195.6(4)	0.01283(12)	58.4(8)	
1234.4(6)	0.01031(11)	80.6(12)	A$_2$ 1229(LO), E 1226(LO)
1606	0.0002	40	
1875	0.00027	52	

Carbonates have been grouped into calcite (CaCO$_3$) and dolomite (Ca$_{0.5}$Mg$_{0.5}$CO$_3$) whose Mie fit results are presented in Tables 2 and 3, respectively. Limestone is prevalent in nature, made up primarily by calcite with some magnesium doping.[53] There is much IR mode work on calcite[33,47−50,52,54−56] and dolomite.[49,50,54,56,57] Calcite has a uniaxial crystal structure making it birefringent.

Since many of the vibrations of calcite and dolomite are localized within the CO$_3^{2-}$ group, the table assignments refer to this entity. A plot of the positions of the carbonate ν_4 versus the position of the ν_2 can be very revealing regarding the metal associated with the carbonate.[4] Both calcite and dolomite have strong and narrow combination bands evident in our spectra and both have their strongest peak, ν_3, in the ~1410−1430 cm^{-1} region, which suffer line shape broadening and distortion due to particle saturation effects.[32] Certain combinations, $\nu_1 + \nu_3$ and $2\nu_3$, have been assigned to multiple peaks, which is consistent with past assignments for these combination bands.[52,55,58,59]

Table 2. Calcite Mie Fit Parameters of the Average of 7 Particle Spectra with Estimated Standard Deviations in Parentheses As Least Significant Figures; the Fitted Radius Was 1.7632(10) μm and ε_0 = 2.467

ν (cm^{-1})	A	Γ (cm^{-1})	assignment/experimental ν (cm^{-1})[47−49]
710.81(16)	0.0033(2)	4.3(4)	E_u ν_4 712, 712
802.9(7)	0.0265(5)	52.4(15)	
847.3(8)	0.0164(4)	43.4(16)	
872.5(2)	0.0102(2)	14.4(5)	A_{2u} ν_2 872, 876
959.7(15)	0.0191(4)	97(3)	
1054.3(11)	0.0199(3)	93(2)	A_{1u} ν_1 1056
1123.9(11)	0.0187(3)	95(2)	
1205.9(10)	0.0187(3)	100(2)	
1370.8(4)	0.0262(2)	67.9(10)	
1293.5(7)	0.0194(2)	84.3(15)	
1425.9(5)	0.0199(2)	58.7(10)	E_u ν_3 1407, 1410(TO), 1435
1477.1(4)	0.01508(19)	48.9(9)	
1523.9(4)	0.01085(14)	45.56308	E_u ν_3 1550(LO)
1793.97925	0.000586372	8.808548	ν_1 + v_4 1812
2511.9(6)	0.000577(19)	27.6(13)	ν_1 + ν_3 2545
2583(5)	0.000081(17)	31(9)	ν_1 + ν_3
2850(2)	0.000065(11)	20(5)	2ν_3
2871.7(15)	0.000152(13)	26(3)	2ν_3 2873
2929(5)	0.000111(15)	47(9)	2ν_3
2975(3)	0.000057(10)	22(5)	2ν_3

Table 3. Dolomite Mie Fit Parameters of the Average of 9 Particle Spectra with Estimated Standard Deviations in Parentheses As Least Significant Figures; the Fitted Radius Was 1.5935(7) μm and ε_0 = 2.425

ν (cm^{-1})	A	Γ (cm^{-1})	assignment/experimental ν (cm^{-1})[49,50,52]
727.7(3)	0.00378(18)	5.9(4)	E_u ν_4 728, 729, 730
796.8(4)	0.0229(4)	36.5(8)	
836.5(6)	0.0218(4)	49.8(12)	
880.8(2)	0.0201(2)	25.5(4)	A_u ν_2 879, 881, 853
1004.3(11)	0.0348(4)	143(2)	
1108.3(5)	0.0336(3)	89.6(10)	
1178.5(8)	0.0168(2)	88.4(16)	A_u ν_1 1100
1066.1(9)	0.0110(2)	59.0(18)	
1296.3(6)	0.02248(19)	99.2(12)	
1396.3(4)	0.02270(18)	80.3(9)	
1440.1(3)	0.02049(17)	57.8(7)	E_u ν_3 1435, 1446, 1450
1478.4(4)	0.01218(14)	44.4(7)	
1511.5(4)	0.00904(12)	40.8(8)	
1545.2(5)	0.00765(9)	52.1(10)	E_u ν_3 1580
1814	0.00048	25	ν_1 + ν_4 1818
2527.7(11)	0.000567(18)	48(2)	ν_1 + ν_3 2525, 2530
2573(4)	0.000154(16)	45(7)	ν_1 + ν_3
2628(3)	0.000121(13)	37(6)	ν_1 + ν_3
2892(3)	0.000155(12)	40.5(5)	2ν_3
2948(11)	0.000038(12)	40(20)	2ν_3 2923
3011(5)	0.000029(8)	20(8)	2ν_3

Table 4. Illite Clay Mie Fit Parameters of the Average of 5 Particle Spectra with Estimated Standard Deviations in Parentheses As Least Significant Figures; the Fitted Radius Was 1.7672(5) μm and ε_0 = 2.5

ν (cm^{-1})	A	Γ (cm^{-1})	assignment/experimental ν (cm^{-1})[61]
			688
			753
			778
795.7(7)	0.00350(9)	38.2(14)	799
829.2(15)	0.00087(7)	26(3)	830
			876
915.5(3)	0.01111(9)	62.5(7)	914
982.49(15)	0.02318(8)	60.1(3)	1003
1049.51(15)	0.01824(7)	56.9(3)	1030
1017.87(17)	0.01465(7)	50.7(3)	
1095.5(2)	0.01193(6)	59.0(4)	1087
1143.1(5)	0.00491(5)	65.3(9)	1119, 1169
1420	0.00025	30	1432
			1623
3270(3)	0.000396(6)	238(6)	OH stretch of H_2O
3423(3)	0.000181(5)	146(5)	OH stretch of H_2O
3560.2(12)	0.000137(3)	75(2)	OH stretch of H_2O
3607.0(5)	0.000151(2)	43.8(9)	OH^- stretch
3634.9(7)	0.0000776(18)	36.6(12)	OH^- stretch

Table 5. Montmorillonite Clay Mie Fit Parameters of the Average of 8 Particle Spectra with Estimated Standard Deviations in Parentheses As Least Significant Figures; the Fitted Radius Was 1.8159(9) μm and ε_0 = 2.5

ν (cm^{-1})	A	Γ (cm^{-1})	assignment/experimental ν (cm^{-1})[61]
			711
792.9(6)	0.00327(13)	19.9(11)	797
814.3(8)	0.00356(14)	27.5(15)	
842.3(7)	0.00378(13)	28.8(14)	848
915.1(8)	0.00432(12)	38.2(15)	884, 919
1019.6(3)	0.03662(16)	83.6(5)	1021
1069.1(3)	0.02330(14)	72.8(6)	1041, 1056
1121.1(4)	0.01305(11)	64.9(8)	1120
1169.2(5)	0.00824(9)	62.5(10)	1152, 1174
1221.9(6)	0.00409(7)	52.9(13)	
1450	0.0001	60	1460
			1647
3275(3)	0.000403(10)	162(6)	OH stretch of H_2O
3398(2)	0.000326(8)	133(5)	OH stretch of H_2O
3507(2)	0.000230(7)	115(5)	OH stretch of H_2O
3618.3(7)	0.000253(4)	54.8(13)	OH^- stretch

Clays can vary over a wide variety of structure and constituents, so here they are grouped into three different types:[60] illite $[(K,H_3O)(Al,Mg,Fe)_2(Si,Al)_4O_{10}[(OH)_2,(H_2O)]$ (Table 4), montmorillonite $[(Na,Ca)_{0.33}(Al,Mg)_2Si_4O_{10}(OH)_2 nH_2O]$ (Table 5), and kaolinite $[Al_2Si_2O_5(OH)_4]$ (Table 6). There has been work on the IR modes of kaolinite,[57,60−65] Illite,[57,60,61,63] and monmorillonite.[57,60,61,63] Kaolinite is the most structured and crystalline of the clays considered here and is distinguishable via its crystalline OH^- stretches, which are much narrower compared with illite and montmorillonite (broadened due to the presence of water, see Figure 2 in the region 3600−3700 cm^{-1}).

Because of their variability, montmorillonite and illite are less ordered, whereas kaolinite is biaxial and trirefringent. Also, on close inspection of the montmorillonite and illite spectra, aliphatic C−H stretches are barely visible at ~2918 and ~2850 cm^{-1}. Though these features are not prominent in the spectra, they do indicate a small presence of organic carbon chains. They were not fit because they are small, not part of the clay

Table 6. Kaolinite Clay Mie Fit Parameters of the Average of 9 Particle Spectra with Estimated Standard Deviations in Parentheses As Least Significant Figures; the Fitted Radius Was 1.9717(9) μm and ε_0 = 2.499

ν (cm^{-1})	A	Γ (cm^{-1})	assignment/experimental ν (cm^{-1})[64,65]
704.4(5)	0.00350(13)	17.5(8)	697
757.6(17)	0.00034(7)	11(3)	SiO_2 755
796.1(8)	0.00080(7)	12.5(15)	SiO_2 789
915.44(17)	0.00621(7)	21.6(3)	OH-deformation 912
938.9(2)	0.00329(6)	18.3(5)	OH-deformation 937
1008.62(19)	0.00891(7)	33.7(4)	Si−O stretch 1007
1044.71(16)	0.01646(8)	45.6(3)	Si−O stretch 1031
1078.4(3)	0.00773(7)	42.7(5)	Si−O stretch
1120.1(2)	0.00624(5)	38.4(5)	Si−O stretch 1115
3442(2)	0.000228(6)	133(5)	OH stretch of H_2O
3533.2(15)	0.000190(5)	80(3)	OH stretch of H_2O
3590.6(8)	0.000166(4)	45.8(15)	OH stretch of H_2O
3616.8(3)	0.000176(2)	15.2(3)	OH^- stretch 3620, 3620
3648.2(3)	0.000248(3)	25.3(4)	OH^- stretch 3653, 3651
3670.1(4)	0.000151(3)	20.4(5)	OH^- stretch 3669, 3668
3689.9(2)	0.000235(2)	16.0(2)	OH^- stretch 3696, 3694

spectrum, and have been addressed with a hydrocarbon calibrant.

Gypsum is a trirefringent crystal, which has a unit cell formula $CaSO_4 \cdot 2H_2O$. The Mie fit parameters are given in Table 7. There has been work on the IR modes.[33,66−69] The strongest phonon is not quite as strong as those of carbonates and quartz, which leaves the strong band less distorted by particle saturation effects. The water within the unit cell is crystalline, which is evident by the sharp H−O−H water bends at ~1624 and 1688 cm^{-1} and with the OH^- stretches above 3400 cm^{-1}.

Organics no doubt exist as a wide range of molecules on dust. Initially organic molecules are part of living organisms (appear yeast-like), but over time the hydrophilic portions of the biological molecules are slowly taken away by natural chemical processes, eventually leaving behind hydrocarbon chains on geologic time scales. These carbon chains are finally thermally driven off the inorganic substrate[35] ending the cycle. There are, no doubt, a rich array of molecules between these extremes, which will require more study before suitable calibrants can be chosen. In the meantime, we have chosen the spectra of ~4 μm polyethylene $[CH_3(CH_2)_{n\approx40}CH_3]$ microspheres (Table 8) and live single yeast cells (Table 9) as calibrating groups. Polyethylene is amorphous, unlike most of the mineral calibrants, and does not suffer from the various orientation or strong phonon effects of the minerals. The polyethylene particles are our best calibrant, being amorphous and spherical. There exist IR studies of long chain hydrocarbons[70−72] showing that the IR spectrum is dominated by CH_2 stretches. Yeast[23] is chosen as a typical live biological calibrant possessing prominent bands including those for protein (amide I and II), lipid carbon chains, and hydrogen bonded water.[73−77] The bread yeast cells match the size of our plasmonic mesh holes very well.

Table 7. Gypsum Mie Fit Parameters of the Average of 8 Particle Spectra with Estimated Standard Deviations in Parentheses As Least Significant Figures; the Fitted Radius Was 2.0747(9) μm and ε_0 = 2.304

ν (cm^{-1})	A	Γ (cm^{-1})	assignment/experimental ν (cm^{-1})[66]
812.3(10)	0.00408(14)	41(2)	
848.1(13)	0.00290(13)	43(3)	
995.7(6)	0.00951(12)	69.2(12)	
939.1(12)	0.00544(13)	70(2)	
1033.0(7)	0.00438(9)	44.8(13)	ν_1 SO_4^{2-} A_u E‖b1005(TO)
1068.5(4)	0.01228(11)	60.0(7)	
1104.0(2)	0.01539(10)	47.0(5)	ν_1 SO_4^{2-} A_u 1105(LO)
1135.0(3)	0.01113(10)	42.0(5)	ν_3 SO_4^{2-} A_u 1128(TO), B_u E‖c 1135(TO), B_uE⊥c 1113(TO)
1167.79(20)	0.01424(8)	48.5(4)	ν_3 SO_4^{2-} A_u 1193(LO), B_u E‖c 1203(LO) B_uE⊥c 1178(LO)
1618.2(2)	0.001270(19)	21.9(5)	ν_2 H_2O 1625(TO), 1633(LO)
1683.2(7)	0.000189(11)	11(1)	ν_2 H_2O 1688(TO), 1690(LO)
2117(5)	0.000032(8)	23(8)	
2208(3)	0.000214(13)	63(5)	
2260(4)	0.000240(15)	84(7)	
3169(2)	0.000482(10)	161(5)	
3245.1(9)	0.000464(7)	84.0(19)	
3329.5(7)	0.000982(9)	104.1(13)	v_1 H_2O B_u E‖c 3390(TO), B_u E⊥c 3388(TO)
3400.2(4)	0.001281(8)	82.1(8)	v_1 H_2O B_u E‖c 3425(LO), B_u E⊥c 3425(LO)
3456.0(8)	0.000387(7)	61.1(15)	v_1 H_2O A_u 3438(TO), 3439(LO)
3500.8(6)	0.000502(6)	58.8(11)	v_3 H_2O A_u 3538(TO)
3559.8(4)	0.000590(6)	59.7(9)	v_3 H_2O A_u 3563(LO), B_u E‖c 3475(TO), 3477(LO)

Table 8. Polyethylene Mie Fit Parameters of the Average of 12 Particle Spectra with Estimated Standard Deviations in Parentheses As Least Significant Figures; the Fitted Radius Was 1.967(4) μm and ε_0 = 2.21

ν (cm^{-1})	A	Γ (cm^{-1})	assignment/experimental ν (cm^{-1})
2910.07(15)	0.001072(8)	31.9(3)	CH_2 asym. stretch
2845.1(2)	0.000755(7)	32.7(5)	CH_2 sym. stretch
1717.1(17)	0.000069(12)	14(3)	impurity
1461.1(6)	0.00043(2)	18.0(12)	CH_2 bend

■ MIE–BRUGGEMAN MODEL FOR VOLUME FRACTIONS

Once a complex index of refraction of each calibrant is available, they can be combined with a Mie–Bruggeman model to determine the volume fraction of each component in the average spectrum of dust. The spectra of all 63 dust particles from our laboratory air were averaged for comparison to this model in a manner similar to the averaging of the calibrants. An extension of Mie theory is employed with Bruggeman Effective Medium Theory[3,78−80] (Mie–Bruggeman theory) by taking the refractive index of each calibrant and combining them into a single effective refractive index. The central relation of Bruggeman theory takes the following form

$$\sum_i f_i \frac{\varepsilon_i - 2\varepsilon_{\text{eff}}}{\varepsilon_i + 2\varepsilon_{\text{eff}}} = 0 \tag{4}$$

where ε_i is the permittivity (dielectric function) of each material and f_i is its volume fraction. Since the effective dielectric is difficult to solve analytically, an iterative approach is used with

Table 9. Yeast Mie Fit Parameters of the Average of 21 Single Live Yeast Cell Spectra with Estimated Standard Deviations in Parentheses As Least Significant Figures; the Radius was 2.0128(12) μm and ε_0 = 1.759

ν (cm^{-1})	A	Γ (cm^{-1})	assignment/experimental ν (cm^{-1})
3477.2(12)	0.000642(11)	94(2)	OH stretch of H_2O
3378.7(8)	0.001651(15)	126.3(17)	OH stretch of H_2O
3280.6(7)	0.001873(16)	116.1(14)	amide A
3165.9(14)	0.001637(18)	176(3)	OH stretch of H_2O
2960(3)	0.000031(5)	13(3)	CH_3 stretch
2922.8(8)	0.000534(11)	51.9(15)	CH_3 asymmetric stretch
2859.6(16)	0.000169(9)	38(3)	CH_3 symmetric stretch
1647.0(4)	0.00527(5)	59.3(8)	amide I
1540.1(6)	0.00563(6)	82.5(13)	amide II
1453.1(12)	0.00246(6)	69(2)	CH_2 bend
1391.5(10)	0.00482(8)	85.0(19)	OCO stretch
1325.2(12)	0.00369(8)	78(2)	amide III?
1258.4(10)	0.00538(10)	82(2)	asym. PO_2^-
1207.4(11)	0.00407(10)	67(2)	
1152.4(9)	0.00365(9)	50.9(19)	
1113.9(8)	0.00486(11)	52.0(16)	
1080.9(9)	0.00264(10)	34.8(18)	sym PO_2^-, C−OH bend
1041.7(5)	0.017423(16)	83.0(11)	
990.5(9)	0.00765(15)	65.3(18)	
941(2)	0.00289(15)	59(4)	
847(2)	0.00110(12)	27(4)	
818(2)	0.00106(13)	26(5)	

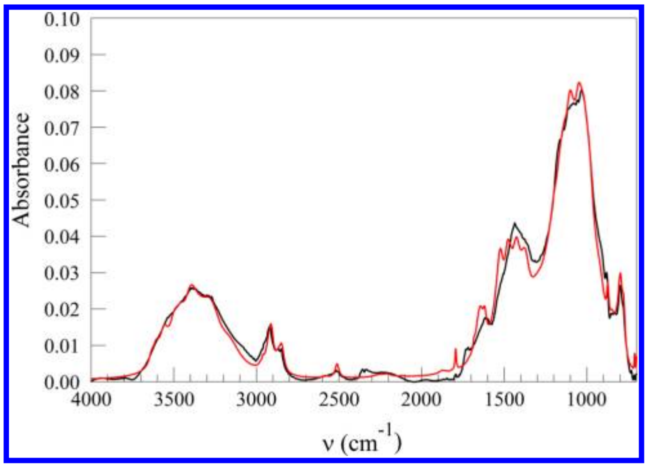

Figure 4. IR spectrum of the average of 63 dust particles from our lab air (black). This spectrum was fit with a Mie−Bruggeman model (red) that adjusted the volume fraction of each component and used the calibrating dielectric functions in Tables 1−9.

an intitial guess of $\varepsilon_{\mathrm{eff}_o} = \sum_{i=0}^{n-1} f_i \varepsilon_i$, where each ε_i was determined by fitting the calibrant's average spectrum in the previous section. Equation 4 is rearranged into an iterative formula

$$\varepsilon_{\mathrm{eff},k} = \frac{\sum_{i=0}^{n-1} \frac{f_i \varepsilon_i}{\varepsilon_i + 2\varepsilon_{i,k-1}}}{\sum_{i=0}^{n-1} \frac{f_i}{\varepsilon_i + 2\varepsilon_{i,k-1}}} \tag{5}$$

where each successive k is the next iteration of the effective dielectric. Convergence was observed in <10 iterations. An effective dielectric is obtained for any given set of volume fractions, which is used with Mie theory to predict the spectrum of the mixed particle.

A home-written Fortran program performed an unweighted nonlinear least-squares fit varying the volume fractions using a grid search method[38] until an optimized fit of the average dust spectrum of 63 particles was obtained as shown in Figure 4. At each grid step of a fitted variable, the program renormalized the volume fractions so that they always added up to 100% (this feature is not available in standard nonlinear least-squares fitting packages). The estimated standard deviation of the fit was computed by summing the squares of deviations between the average spectrum of 63 dust particles and the best fit Mie−Bruggeman model assuming equal weights at each wavenumber step. The value of the estimated standard deviation of the fit [square root of the sum of the squares of the deviations divided by the degrees of freedom (number of spectral points minus the number of parameters fit)] was 0.0027 in absorbance units, which is ~3% of the maximum peak. The uncertainties of all parameters were estimated by calculating the diagonal elements of the variance-covariance matrix at the end of the last iteration (which requires knowledge of the standard deviation of the fit and involves calculating the sums over the spectral data points of the squares of the first partial derivatives of the fitted spectrum with respect to each parameter). The best fit volume fractions and their uncertainties (estimated standard deviations from the diagonal elements of the variance-covariance matrix) are presented in Table 10. Illite constitutes the largest mineral volume fraction in our lab air at 30%. The other two clay groups could not be discerned with statistical significance. The two organic groups combine to give 27%, which is consistent with detection in 68% of the individual dust particle spectra. Quartz represents only 19% of the volume even though it occurs (or was detected) in 53% of the individual dust particles. This suggests a distribution of quartz in the individual particles of a dust sample that would be interesting to determine by single particle studies and possibly characteristic of local areas. Gypsum registers at 14%, while both carbonate groups sum to 11%. Surprisingly at 1791 and 2536 cm^{-1}, there are small peaks that the fit shows to be combination bands for calcite. The fact that the method of taking spectra of individual particles and averaging them together, while still retaining such small details, is an encouraging one.

Table 10. Volume Fractions from a Nonlinear Least Squares Fit to the Mie-Bruggeman Model of the Average Dust Spectrum from Our Lab Air; Estimated Standard Deviations Are Given in Parentheses As Least Significant Figures; the Fitted Radius Was 1.906(2) μm

calibrant	volume fraction
illite clay	0.300(10)
live yeast	0.186(7)
quartz	0.186(6)
gypsum	0.137(7)
calcite	0.103(2)
polyethylene	0.081(5)
dolomite	0.006(2)
montmorillonite clay	0.000(12)
kaolinite clay	0.000(6)

While the overall fit is reasonable, there are some deficiencies. The region from 1500 to 1700 cm^{-1} has the largest deviations. This is a region where we expect to find organic molecules (the amide I band of proteins, C═O stretches of ester-linked fat chains, and O−C−O stretches). We have found various organic bands in this region in the spectra of individual dust particles.[34] In fact, parallel work is currently underway to use this IR region with clustering analysis in order to identify more organic groups of molecules. More data on individual dust particles will, however, be required. Notice that new calibrants can readily be added to make the current model better. Perhaps some of these groups will be the tar of decaying leaves and the humic acid in dirt (materials that make soil brown).

CONCLUSIONS

A spectral model (Mie−Bruggeman) has been presented, which predicts the orientationally averaged, infrared spectra of individual mixed-composition particles or the average spectrum of collections of such particles. The Mie-Bruggeman model is general, but the calibration is specific. It requires calibrants that cover the components in a mixture of interest, which in this case was the dust from our laboratory air. Calibrants were selected that pertain to airborne dust including quartz, calcite, dolomite, three clays, gypsum, polyethylene, and living organic material (yeast cells). If important components are missing, then there will be systematic errors in the model's results. However, as new materials are found in samples, new calibrations can be obtained and added to the present model. The scatter-free IR spectra of 94 individual particles of nine different calibrating materials were recorded, and the orientationally averaged spectra of each of nine calibrants were analyzed to obtain the dielectric functions for each calibrant (as presented in Tables 1−9). The dielectric functions (being orientationally averaged) are the solid-state analogues of quantities like molar extinction coefficients or absolute cross-sections, and as such may be useful to investigators of their own accord. The Mie−Bruggeman model did a reasonable job modeling the average spectrum of dust particles from our lab air. The lab air particles were found to have volume percentages of 27% organic matter (19% yeast-like and 8% polyethylene-like), 30% clay (mostly Illite), 19% quartz, 14% gypsum, and 11% carbonates (10% calcite and 1% dolomite). This shows that the model has potential for quantitative analysis, but we do not yet know the absolute accuracy of the volume fractions that were determined. In the near future, work would benefit from a greater variety of organic calibrants and calibrants for less prevalent mineral components. This Mie−Bruggeman method shows potential as a spectral alternative to the traditional chemical analyses; however, that goal has not yet been realized. Demonstration of that potential awaits testing on samples with single particles of known volume fractions, which, as far as we know, would have to be synthesized.

Further into the future, we plan to develop an extension of this model that allows for anisotropic dielectric functions (orientation of crystal transition moments). It would basically allow for light to be shined on a particle at any specific orientation (incorporating any averaging of the spectrometer/microscope optics). The advent of such a modification would enable the Mie−Bruggeman method to determine the volume fractions of individual particles. This would be particularly welcome when the particles are rare and hard to obtain. Such a capability would enable the determination of component distributions, not just the averages as with the current model.

ASSOCIATED CONTENT

Supporting Information

IR spectra of individual calibrating particles. This material is available free of charge via the Internet at http://pubs.acs.org.

AUTHOR INFORMATION

Corresponding Author

*(J.V.C.) Phone: 614-292-9489. E-mail: coe.1@osu.edu.

Notes

The authors declare no competing financial interest.

ACKNOWLEDGMENTS

We thank the National Science Foundation for support of this work under grant number CHE 1213293.

REFERENCES

(1) Bohren, C. F.; Huffman, D. R. *Absorption and Scattering of Light by Small Particles*; Wiley-VCH: Berlin Germany, 2007.

(2) van de Hulst, H. C. *Light Scattering by Small Particles*; Dover: New York, 1981.

(3) Bruggeman, D. A. G. The Calculation of Various Physical Constants of Heterogeneous Substances. I. The Dielectric Constants and Conductivities of Mixtures Composed of Isotropic Substances. *Ann. Phys.* **1935**, *24*, 636−664.

(4) Cilwa, K. E.; McCormack, M.; Lew, M.; Robitaille, C.; Corwin, L.; Malone, M. A.; Coe, J. V. Scatter-Free IR Absorption Spectra of Individual, 3−5 Micron, Airborne Dust Particles Using Plasmonic Metal Microarrays: A Library of 63 Spectra. *J. Phys. Chem. C* **2011**, *115*, 16910−16919.

(5) Eastwood, P. *Particulate Emissions from Vehicles*; John Wiley & Sons: Chichester, U.K., 2008.

(6) Hinds, W. C. *Aerosol Technology: Properties, Behavior, and Measurement of Airborne Particles*; J. Wiley: New York, 1982.

(7) Jung, H.-J.; Malek, M. A.; Ryu, J.; Kim, B.; Song, Y.-C.; Kim, H.; Ro, C.-U. Speciation of Individual Mineral Particles of Micrometer Size by the Combined Use of Attenuated Total Reflectance-Fourier Transform-Infrared Imaging and Quantitative Energy-Dispersive Electron Probe X-ray Microanalysis Techniques. *Anal. Chem.* **2010**, *82*, 6193−6202.

(8) Wopenka, B.; Swan, P. D. Micro-FTIR Measurements on Individual Interplanetary Dust Particles. *Mikrochim. Acta* **1988**, *1*, 183−187.

(9) Rotundi, A.; Baratta, G. A.; Borg, J.; Brucato, J. R.; Busemann, H.; Colangeli, L.; D'Hendecourt, L.; Djouadi, Z.; Ferrini, G.; Franchi, I. A. Combined Micro-Raman, Micro-Infrared, and Field Emission Scanning Electron Microscope Analyses of Comet 81P/Wild 2 Particles Collected by Stardust. *Meteorit. Planet. Sci.* **2008**, *43*, 367−397.

(10) Savage, B. D.; Mathis, J. S. Observed Properties of Interstellar Dust. *Annu. Rev. Astron. Astrophys.* **1979**, *17*, 73−111.

(11) Sandford, S. A.; Walker, R. M. Laboratory Infrared Transmission Spectra of Individual Interplanetary Dust Particles From 2.5 To 25 Microns. *Astrophys. J.* **1985**, *291*, 838−851.

(12) Raynal, P. I.; Quirico, E.; Borg, J.; Deboffle, D.; Dumas, P.; d'Hendecourt, L.; Bibring, J. P.; Langevin, Y. Synchrotron Infrared Microscopy of Micron-Sized Extraterrestrial Grains. *Planet. Space Sci.* **2000**, *48*, 1329−1339.

(13) Sokolik, I. N.; Toon, O. B.; Bergstrom, R. W. Modeling the Radiative Characteristics of Airborne Mineral Aerosols at Infrared Wavelengths. *J. Geophys. Res.* **1998**, *103*, 8813−8826.

(14) Maskey, S.; Kang, T.; Jung, H.-J.; Ro, C.-U. Single-Particle Characterization of Indoor Aerosol Particles Collected at an Underground Shopping Area in Seoul, Korea. *Indoor Air* **2011**, *21*, 12−24.

(15) Hoidale, G. B.; Blanco, A. J. Infrared Absorption Spectra of Atmospheric Dust Over An Interior Desert Basin. *Pure Appl. Geophys.* **1969**, *74*, 151−164.

(16) Blanco, A. J.; Hoidale, G. B. Microspectrophotometric Technique For Obtaining Infrared Spectrum of Microgram Quantities of Atmospheric Dust. *Atmos. Environ.* **1968**, *2*, 327−330.

(17) Laskin, A.; Cowin, J. P.; Iedema, M. J. Analysis of Individual Environmental Particles Using Modern Methods of Electron Microscopy and X-Ray Microanalysis. *J. Electron Spectrosc. Relat. Phenom.* **2006**, *150*, 260−274.

(18) Farfel, M.; DiGrande, L.; Brackbill, R.; Prann, A.; Cone, J.; Friedman, S.; Walker, D.; Pezeshki, G.; Thomas, P.; Galea, S. An Overview of 9/11 Experiences and Respiratory and Mental Health Conditions among World Trade Center Health Registry Enrollees. *J. Urban Health* **2008**, *85*, 880−909.

(19) Bell, M. L.; Ebisu, K.; Peng, R. D.; Samet, J. M.; Dominici, F. Hospital Admissions and Chemical Composition of Fine Particle Air Pollution. *Am. J. Respir. Crit. Care Med.* **2009**, *179*, 1115−1120.

(20) Dominici, F.; McDermott, A.; Zeger, S. L.; Samet, J. M. National Maps of the Effects of Particulate Matter on Mortality: Exploring Geographical Variation. *Environ. Health Perspect.* **2003**, *111*, 39−43.

(21) Peng, R. D.; Chang, H. H.; Bell, M. L.; McDermott, A.; Zeger, S. L.; Samet, J. M.; Dominici, F. Coarse Particulate Matter Air Pollution and Hospital Admissions for Cardiovascular and Respiratory Diseases Among Medicare Patients. *JAMA* **2008**, *299*, 2172−2179.

(22) Polichetti, G.; Cocco, S.; Spinali, A.; Trimarco, V.; Nunziata, A. Effects of Particulate Matter (PM_{10}, $PM_{2.5}$, and PM_1) on the Cardiovascular System. *Toxicology* **2009**, *261*, 1−8.

(23) Malone, M. A.; Prakash, S.; Heer, J. M.; Corwin, L. D.; Cilwa, K. E.; Coe, J. V. Modifying Infrared Scattering Effects of Single Yeast Cells with Plasmonic Metal Mesh. *J. Chem. Phys.* **2010**, *133*, 185101−185107.

(24) Heer, J.; Corwin, L.; Cilwa, K.; Malone, M. A.; Coe, J. V. Infrared Sensitivity of Plasmonic Metal Films with Hole Arrays to Microspheres In and Out of the Holes. *J. Phys. Chem. C* **2010**, *114*, 520−525.

(25) Malone, M. A.; Cilwa, K. E.; Luthra, A.; McCormack, M.; Lioi, D.; Coe, J. V. Plasmonics under the Infrared Microscope: Sensing and Spectra of Single Particles Using Metal Film Hole Arrays. *Photonics and Optoelectronics (SOPO)* **2012**, *1*, 21−23.

(26) Malone, M. A.; McCormack, M.; Coe, J. V. Single Airborne Dust Particles using Plasmonic Metal Films with Hole Arrays. *J. Phys. Chem. Lett.* **2012**, *3*, 720−724.

(27) Coe, J. V.; Heer, J. M.; Teeters-Kennedy, S.; Tian, H.; Rodriguez, K. R. Extraordinary Transmission of Metal Films with Arrays of Subwavelength Holes. *Annu. Rev. Phys. Chem.* **2008**, *59*, 179−202.

(28) Coe, J. V.; Rodriguez, K. R.; Teeters-Kennedy, S.; Cilwa, K.; Heer, J.; Tian, H.; Williams, S. M. Metal films with Arrays of Tiny Holes: Spectroscopy with Infrared Plasmonic Scaffolding. *J. Phys. Chem. C* **2007**, *111*, 17459−17472.

(29) Coe, J. V.; Williams, S. M.; Rodriguez, K. R.; Teeters-Kennedy, S.; Sudnitsyn, A.; Hrovat, F. Extraordinary IR Transmission with Metallic Arrays of Subwavelength Holes. *Anal. Chem.* **2006**, *78*, 1384−1390.

(30) Williams, S. M.; Rodriguez, K. R.; Teeters-Kennedy, S.; Shah, S.; Rogers, T. M.; Stafford, A. D.; Coe, J. V. Scaffolding for Nanotechnology: Extraordinary Infrared Transmission of Metal Microarrays for Stacked Sensors and Surface Spectroscopy. *Nanotechnology* **2004**, *15*, S495−S503.

(31) Hobert, H. Characterization Of Atmospheric Dust Sediments By Using Infrared-Spectroscopy: Dust Spectra And An Analytical Model. *Vib. Spectrosc* **1995**, *9*, 169−179.

(32) Ravi, A.; Malone, M. A.; Luthra, A.; Lioi, D.; Coe, J. V. Spectral Challenges of Individual Wavelength-Scale Particles: Strong Phonons and Their Distorted Lineshapes. *Phys. Chem. Chem. Phys.* **2013**, *15*, 10307−10315.

(33) Long, L. L.; Querry, M. R.; Bell, R. J.; Alexander, R. W. Optical Properties of Calcite and Gypsum in Crystalline and Powdered Form in the Infrared and Far-Infrared. *Infrared Phys.* **1993**, *34*, 191−201.

(34) Robitaille, C. I. Characterization of Particulate Matter Containing Various Organic Components. BS, The Ohio State University, 2011.

(35) Xie, W.; Gao, Z.; Liu, K.; Pan, W.-P.; Vaia, R.; Hunter, D.; Singh, A. Thermal Characterization of Organically Modified Montmorillonite. *Thermochim. Acta* **2001**, *367−368*, 339−350.

(36) Barber, P. W., Chang, R. K., Eds. *Optical Effects Associated with Small Particles*; World Scientific Publishing Co. Pte. Ltd.: Singapore, 1988.

(37) Heer, J. M. FDTD Modeling of the Spectroscopy and Resonances of Thin Films and Particles on Plasmonic Nickel Mesh. Ph.D. Thesis, The Ohio State University, 2010.

(38) Bevington, P. W. *Data Reduction and Error Analysis for the Physical Sciences*; McGraw-Hill: New York, 1969.

(39) Zicovich-Wilson, C. M.; Pascale, F.; Roetti, C.; Saunders, V. R.; Orlando, R.; Dovesi, R. Calculation of the Vibration Frequencies of α-Quartz: The Effect of Hamiltonian and Basis Set. *J. Comput. Chem.* **2004**, *25*, 1873−1881.

(40) Steyer, T. R.; Day, K. L.; Huffman, D. R. Infrared Absorption by Small Amorphous Quartz Spheres. *Appl. Opt.* **1974**, *13*, 1586−1590.

(41) Popova, S. I.; Tolstykh, T. S.; Vorobev, V. T. Optical Characteristics of Amorphous Quartz in the 1400−200 cm^{-1} Region. *Opt. Spectrosc.* **1972**, *33*, 444−445.

(42) Peterson, J. T.; Weinman, J. A. Optical Properties of Quartz Dust Particles at Infrared Wavelengths. *J. Geophys. Res.* **1969**, *74*, 6947−6952.

(43) Spitzer, W. G.; Kleinman, D. A. Infrared Lattice Bands of Quartz. *Phys. Rev.* **1961**, *121*, 1324−1335.

(44) Gervais, F.; Piriou, B. Temperature Dependence of Transverse and Longitudinal Optic Modes in the Alpha and Beta Phases of Quartz. *Phys. Rev. B* **1975**, *11*, 3944−3950.

(45) Thomas, M.; Gautier, C. Investigations of the March 2006 African Dust Storm Using Ground-Based Column-Integrated High Spectral Resolution Infrared (8−13 Microns) and Visible Aerosol Optical Thickness Measurements: 2. Mineral Aerosol Mixture Analyses. *J. Geophys. Res.* **2009**, *114*, D11202/11201−11212.

(46) Plyler, E. K. Combination Frequencies of the Infra-red Bands of Quartz. *Phys. Rev.* **1929**, *33*, 48−51.

(47) Lou, D.; Sun, F.; Li, L. Study on Vibrational Modes by Group Theory and Infrared Spectra by DFT for Calcite Crystal. *Chin. Opt. Lett.* **2007**, *5*, 370−372.

(48) Ishigame, M.; Sato, T.; Sakurai, T. Splitting of the TO Mode in Calcite by the Polarization Field. *Phys. Rev. B* **1971**, *3*, 4388−4391.

(49) Gaffey, S. J. Spectral Reflectance of Carbonate Minerals in the Visible and Near Infrared (0.35−2.55 microns): Anhydrous Carbonate Minerals. *J. Geophys. Res.* **1987**, *92*, 1429−1440.

(50) Valenzano, L.; Noël, Y.; Orlando, R.; Zicovich-Wilson, C. M.; Ferrero, M.; Dovesi, R. Ab Initio Vibrational Spectra and Dielectric Properties of Carbonates: Magnesite, Calcite and Dolomite. *Theor. Chem. Acc.* **2007**, *117*, 991−1000.

(51) Poduska, K. M.; Regev, L.; Boaretto, E.; Addadi, L.; Weiner, S.; Kronik, L.; Curtarolo, S. Decoupling Local Disorder and Optical Effects in Infrared Spectra: Differentiating Between Calcites with Different Origins. *Adv. Mater.* **2011**, *23*, 550−554.

(52) Gunasekaran, S.; Anbalagan, G.; Pandi, S. Raman and Infrared Spectra of Carbonates of Calcite Structure. *J. Raman Spectrosc.* **2006**, *37*, 892−899.

(53) Wang, D.; Wallace, A. F.; De Yoreo, J. J.; Dove, P. M. Carboxylated Molecules Regulate Magnesium Content of Amorphous Calcium Carbonates During Calcification. *Proc. Natl. Acad. Sci. U.S.A.* **2009**, *106*, 21511−21516.

(54) Posch, T.; Baier, A.; Mutschke, H.; Henning, T. Carbonates in Space: The Challenge of Low-Temperature Data. *Astrophys. J.* **2007**, *668*, 993−1000.

(55) Lane, M. D. Midinfrared Optical Constants of Calcite and Their Relationship to Particle Size Effects in Thermal Emission Spectra of Granular Calcite. *J. Geophys. Res.* **1999**, *104*, 14099−14108.

(56) Lane, M. D.; Christensen, P. R. Thermal Infrared Emission Spectroscopy of Anhydrous Carbonates. *J. Geophys. Res.* **1997**, *102*, 25581−25592.

(57) Querry, M. Optical Constants of Minerals and Other Materials from the Millimeter to the Ultraviolet. *Chemical Research Development and Engineering Center, Aberdeen Proving Ground*, 1987.

(58) Gillet, P.; McMillan, P.; Schott, J.; Badro, J.; Grzechnik, A. Thermodynamic Properties and Isotopic Fractionation of Calcite from Vibrational Spectroscopy of 18O-Substituted Calcite. *Geochim. Cosmochim. Acta* **1996**, *60*, 3471−3485.

(59) Haas, C.; Ketelaar, J. A. A. The Effective Field and the Frequency of Overtones and Combination Bands in the Vibration Spectra of Crystals. *Physica* **1956**, *22*, 1286−1290.

(60) Hudson, P. K.; Gibson, E. R.; Young, M. A.; Kleiber, P. D.; Grassian, V. H. Coupled Infrared Extinction and Size Distribution Measurements for Several Clay Components of Mineral Dust Aerosol. *J. Geophys. Res.* **2008**, *113*, D01201−01211.

(61) Glotch, T. D.; Rossman, G. R.; Aharonson, O. Mid-Infrared (5−100 Micron) Reflectance Spectra and Optical Constants of Ten Phyllosilicate Minerals. *Icarus* **2007**, *192*, 605−622.

(62) Parthasarathy, G.; Saikia, B. J. Fourier Transform Infrared Spectroscopic Characterization of Kaolinite from Assam and Meghalaya, Northeastern India. *J. Mod. Phys.* **2010**, *1*, 206−210.

(63) Schuttlefield, J. D.; Cox, D.; Grassian, V. H. An Investigation of Water Uptake on Clay Minerals Using ATR-FTIR Spectroscopy Coupled with Quartz Crystal Microbalance Measurements. *J. Geophys. Res.* **2007**, *112*, 303−317.

(64) Tosoni, S.; Doll, K.; Ugliengo, P. Hydrogen Bond in Layered Materials: Structural and Vibrational Properties of Kaolinite by a Periodic B3LYP Approach. *Chem. Mater.* **2006**, *18*, 2135−2143.

(65) Bougeard, D.; Smirnov, K. S.; Geidel, E. Vibrational Spectra and Structure of Kaolinite: A Computer Simulation Study. *J. Phys. Chem. B* **2000**, *104*, 9210−9217.

(66) Takahashi, H.; Maehara, I.; Kaneko, N. Infrared Reflection Spectra of Gypsum. *Spectrochim. Acta, Part A* **1983**, *39*, 449−455.

(67) Aronson, J. R.; Emslie, A. G.; Miseo, E. V.; Smith, E. M.; Strong, P. F. Optical Constants of Monoclinic Anisotropic Crystals: Gypsum. *Appl. Opt.* **1983**, *22*, 4093−4098.

(68) Iishi, K. Phononspectroscopy and Lattice Dynamical Calculations of Anhydrite and Gypsum. *Phys. Chem. Miner.* **1979**, *4*, 341−359.

(69) Hass, M.; Sutherland, G. B. B. M. The Infra-Red Spectrum and Crystal Structure of Gypsum. *Proc. R. Soc. London, Ser. A* **1956**, *236*, 427−445.

(70) Snyder, R. G. Vibrational Study of the Chain Conformation of the Liquid *n*-Paraffins and Molten Polyethylene. *J. Chem. Phys.* **1967**, *47*, 1316−1360.

(71) Snyder, R. G.; Schachtschneider, J. H. A Valence Force Field for Saturated Hydrocarbons. *Spectrochim. Acta* **1965**, *21*, 169−195.

(72) Schachtschneider, J. H.; Snyder, R. G. Normal Coordinate Calculations of Large Hydrocarbon Molecules and Polymers. *J. Polym. Sci.* **1964**, *7*, 99−122.

(73) Saulou, C.; Jamme, F.; Maranges, C.; Fourquaux, I.; Despax, B.; Raynaud, P.; Dumas, P.; Mercier-Bonin, M. Synchrotron FTIR Microspectroscopy of the Yeast *Saccharomyces cerevisiae* after Exposure to Plasma-Deposited Nanosilver-Containing Coating. *Anal. Bioanal. Chem.* **2010**, *396*, 1441−1450.

(74) Jorgensen, P.; Edgington, N. P.; Schneider, B. L.; Rupes, I.; Tyers, M.; Futcher, B. The Size of the Nucleus Increases as Yeast Cells Grow. *Mol. Biol. Cell* **2007**, *18*, 3523−3532.

(75) Ngo-Thi, N. A.; Kirschner, C.; Naumann, D. Characterization and Identification of Microorganisms by FT-IR Microspectrometry. *J. Mol. Struct.* **2003**, *661−662*, 371−380.

(76) Wenning, M.; Seiler, H.; Scherer, S. Fourier-Transform Infrared Microspectroscopy, a Novel and Rapid Tool for Identification of Yeasts. *Appl. Environ. Microbiol.* **2002**, *68*, 4717−4721.

(77) Beauvoit, B.; Liu, H.; Kang, K.; Kaplan, P.; Miwa, M.; Chance, B. Characterization of Absorption and Scattering Properties for Various Yeast Strains by Time-Resolved Spectroscopy. *Cell Biochem. Biophys.* **1993**, *23*, 91−109.

(78) Garcia-Caurel, E.; Bertran, E.; Canillas, A. Application of FTIR Phase-Modulated Ellipsometry to the Characterization of Thin Films on Surface-Enhanced IR Absorption Active Substrates. *Thin Solid Films* **2001**, *398−399*, 99−103.

(79) Stroud, D. The Effective Medium Approximations: Some Recent Developments. *Superlattices Microstruct.* **1998**, *23*, 567−573.

(80) Yang, F.; Bradberry, G. W.; Sambles, J. R. The Study of the Optical Properties of Obliquely Evaporated Nickel Films using IR Surface Plasmons. *Thin Solid Films* **1991**, *196*, 35−46.